

Physical Modeling and Numerical Studies of Three-dimensional Non-equilibrium Multi-temperature Flows

Guiyu Cao,^{1, a)} Hualin Liu,^{2, b)} and Kun Xu^{1, 3, c)}

¹⁾*Department of Mathematics, Hong Kong University of Science and Technology,
Clear Water Bay, Kowloon, Hong Kong*

²⁾*College of Aeronautics and Astronautics, Zhejiang University, Hangzhou,
Zhejiang 310058, China*

³⁾*Department of Mechanical and Aerospace Engineering,
Hong Kong University of Science and Technology, Clear Water Bay, Kowloon,
Hong Kong*

(Dated: 12 October 2018)

For increasingly rarefied flowfields, the Navier-Stokes (NS) equations lose accuracy partially due to the single temperature approximation. To overcome this barrier, a continuum multi-temperature model based on the Bhatnagar-Gross-Krook (BGK) equation coupled with the Landau-Teller-Jeans relaxation model has been proposed for two-dimensional hypersonic non-equilibrium multi-temperature flow computation. In recent study, a two-stage fourth-order gas-kinetic scheme (GKS) has been developed for equilibrium flows, which achieves a fourth-order accuracy in space and time as well as high efficiency and robustness. In this paper, targeting for accurate and efficient simulation of multi-temperature non-equilibrium flows, a high-order three-dimensional multi-temperature GKS is implemented under the two-stage fourth-order framework, with the fourth-order Simpson interpolation rule for the newly emerged source term. Simulations on decaying homogeneous isotropic turbulence, low-density nozzle flow, rarefied hypersonic flow over a flat plate, and type IV shock-shock interaction are used to validate the multi-temperature model through the comparison with experimental measurements. The unified gas kinetic scheme (UGKS) results, and the Direct simulation Monte Carlo (DSMC) solutions will be used as well in some cases for validation. Computational results not only confirm the high-order accuracy and quite robustness of this scheme, but also show the significant improvement on computational efficiency compared with UGKS and DSMC, especially in the near continuum flow regime.

Keywords: Multi-temperature kinetic model; Gas-kinetic method; High-order temporal discretization; Non-equilibrium flow computation.

^{a)}Electronic mail: gcaaaa@connect.ust.hk

^{b)}Electronic mail: hualinliu@zju.eud.cn

^{c)}Electronic mail: makxu@ust.hk

I. INTRODUCTION

The classification of flow regimes is based on the Knudsen number Kn , which is defined as the ratio of the molecular mean free path over a characteristic length scale of the system. The whole flow regime is roughly divided into continuum flow regime ($Kn \leq 0.01$), continuum-transition regime ($0.01 < Kn \leq 10$), and free molecular regime ($Kn > 10$). The Navier-Stokes (NS) equations with linear relations between stress and strain and the Fourier's laws are adequate to model the equilibrium flow in the continuum flow regime. For non-equilibrium flow in the continuum-transition regime, the Navier-Stokes equations are well known to be inadequate. However, this continuum-transition regime is important for many scientific and practical engineering applications, such as the simulation of micro-scale flows and space exploration vehicles¹. Therefore, accurate models with reliable solutions and lower computational costs for non-equilibrium flow are useful for solving the non-equilibrium flow problem in the near continuum regime.

Available numerical schemes for simulating non-equilibrium flow can be classified into particle method and deterministic method. Direct simulation Monte Carlo (DSMC)^{2,3} uses probabilistic simulation to solve the Boltzmann equation, which is a representative of particle method and is widely used for rarefied low simulations. However, in the continuum-transition regime, DSMC requires a great amount of particles and the cell size and time step are limited by the particle mean free path and mean collision time, which is very expensive both in the memory cost and computational time. The deterministic method, such as Discrete Velocity Methods (DVM) or Discrete Ordinate Method (DOM)⁴⁻⁷, solve the Boltzmann or model equations directly with the discretization of particle velocity space. In the continuum-transition regime, the cell size and time step are also constrained by the particle mean free path and mean collision time, make these methods be prohibitively expensive. Recently, the multi-scale numerical scheme unified gas kinetic scheme (UGKS)⁸⁻¹¹ has been developed successfully for monatomic and diatomic gases for entire Knudsen number flow. Different from the splitting process used in DSMC and DVM/DOM methods, the distinguishable feature of UGKS is the coupling of the particle transport and collision, which makes the grid size and time step used in UGKS are not limited by the particle mean free path and collision time, such as those imposed in DSMC and DVM methods. Even though UGKS is the most efficient method for whole flow regime simulation currently, in view of a considerable

number of discrete velocity points to be updated, it is still expensive in the near continuum flow regime than those based on the macroscopic equations. At the same time, for smooth flow, such as those in the boundary layer, a high-order scheme is preferred to get accurate solutions. However, most schemes for the rarefied flow, such as DSMC, DVM/DOM, and UGKS methods, have only at most second-order accuracy.

To study non-equilibrium flow efficiently, an extended Bhatnagar-Gross-Krook (BGK) model coupled with the Landau-Teller-Jeans relaxation model has been proposed for two-dimensional non-equilibrium multi-temperature flow computation^{12,13}. In the continuum flow regime, the corresponding kinetic scheme goes back automatically to the BGK-NS method. On the other hand, this kinetic scheme solves the non-equilibrium translational and rotational flow quite efficiently in the near continuum regime. In recent study, an accurate and robust two-stage fourth-order gas-kinetic scheme (GKS)^{14,15} has been developed for equilibrium flows, which achieves a fourth-order accuracy in space and time, and shows high efficiency and robustness from smooth flow to shock problem. In view of smooth equilibrium region appearing in the non-equilibrium multi-temperature flows, a high-order non-equilibrium GKS based on extended BGK method is preferred for simulating multi-temperature flow efficiently and accurately. In current study, this high-order non-equilibrium GKS is implemented under the previous two-stage fourth-order framework for three-dimensional multi-temperature flows, and the source term is dealt with fourth-order Simpson interpolation rule. Numerical tests from smooth decaying homogeneous isotropic turbulence to challenging hypersonic type IV shock-shock interaction validate current high-order non-equilibrium GKS. This high-order non-equilibrium GKS not only preserves high accuracy and quite robustness through numerical cases, but also shows the significant improvement on computational efficiency in near continuum flow region.

In this paper, details on current extended kinetic model and corresponding macroscopic equations are presented in Section 2. Section 3 gives the construction of this high-order non-equilibrium numerical scheme under two-stage fourth-order framework for solving this extended kinetic model. This is followed by the results and discussion of the non-equilibrium multi-temperature flow computations in Section 4. Discussion and conclusion are shown in the final section.

II. GAS-KINETIC MODELS AND MACROSCOPIC GOVERNING EQUATIONS FOR DIATOMIC GAS

In this section, the extended kinetic model and its derived macroscopic equations in three dimension for diatomic gases are presented.

A. Equilibrium translational and rotational temperature model

By modeling the time evolution of a gas distribution function resulting from the free transport and binary elastic collision, the Boltzmann equation has been constructed for monotonic dilute gas. The simplification of the Boltzmann equation given by the BGK model has the following form¹⁶,

$$\frac{\partial f}{\partial t} + u \frac{\partial f}{\partial x} + v \frac{\partial f}{\partial y} + w \frac{\partial f}{\partial z} = \frac{g - f}{\tau}, \quad (1)$$

where f is the number density of molecules at position (x, y, z) and particle velocity (u, v, w) at time t . The left side of the Eq.(1) denotes the free transport, and the right hand side represents the collision term. The relation between distribution function f and macroscopic variables, such as mass, momentum, energy and stress, can be obtained by taking moments of the distribution function. The collision operator in BGK model shows simple relaxation process from f to a local equilibrium state g , with a characteristic time scale τ related to the viscosity and heat conduction coefficients. The local equilibrium state is a Maxwellian distribution,

$$g = \rho \left(\frac{\lambda}{\pi}\right)^{\frac{K+3}{2}} e^{-\lambda[(u-U)^2 + (v-V)^2 + (w-W)^2 + \xi^2]}, \quad (2)$$

where ρ is the density, (U, V, W) are the macroscopic fluid velocity in the x -, y - and z - directions. Here $\lambda = m/2kT$, m is the molecular mass, k is the Boltzmann constant, and T is the temperature. For three-dimensional equilibrium diatomic gas, the total number of degrees of freedom $K = 2$, the internal variable ξ accounts for the rotational modes as $\xi^2 = \xi_1^2 + \xi_2^2$, and the specific heat ratio $\gamma = (K + 5)/(K + 3)$ is determined.

Based on the above BGK model as Eq.(1), the Euler equations can be obtained for a local equilibrium state with $f = g$. On the other hand, for the Navier-Stokes equations, the stress and Fourier heat conduction terms can be derived with the Chapman-Enskog expansion¹⁷ truncated to the 1st-order as,

$$f = g + Knf_1 = g - \tau\left(\frac{\partial g}{\partial t} + u\frac{\partial g}{\partial x} + v\frac{\partial g}{\partial y} + w\frac{\partial g}{\partial z}\right). \quad (3)$$

For the Burnett and super-Burnett equations, the above expansion can be naturally extended¹⁸, such as $f = g + Knf_1 + Kn^2f_2 + Kn^3f_3 + \dots$. For the above Navier-Stokes solutions, the GKS based on the kinetic BGK model has been well developed¹⁹. In order to simulate the flow with any realistic Prandtl number, a modification of the heat flux in the energy transport is used in this scheme, which is also implemented in the present study.

B. Non-equilibrium translational and rotational temperature model

A single temperature is assumed for translational and rotational modes in the above Navier-Stokes equations. However, it loses accuracy in the simulation of non-equilibrium flow because of the different temperatures for the translational and rotational energy modes. In the following section, an extended BGK model for non-equilibrium rotational energy is constructed and for the 1st time the corresponding three-dimensional macroscopic governing equations are derived.

For non-equilibrium multi-temperature diatomic gas flow, the above-mentioned BGK model can be extended in the following form,

$$\frac{\partial f}{\partial t} + u\frac{\partial f}{\partial x} + v\frac{\partial f}{\partial y} + w\frac{\partial f}{\partial z} = \frac{f^{eq} - f}{\tau} + \frac{g - f^{eq}}{Zr\tau} = \frac{f^{eq} - f}{\tau} + Q_s, \quad (4)$$

where an intermediate equilibrium state f^{eq} different with Eq.(2) is introduced with two temperatures, one for translational temperature and the other for rotational temperature,

$$f^{eq} = \rho\left(\frac{\lambda_t}{\pi}\right)^{3/2}\left(\frac{\lambda_r}{\pi}\right)e^{-\lambda_t[(u-U)^2+(v-V)^2+(w-W)^2]-\lambda_r\xi_r^2}, \quad (5)$$

where $\lambda_t = m/2kT_t$ is related to the translational temperature T_t , and $\lambda_r = m/2kT_r$ accounts for the rotational temperature T_r . Therefore, the right hand side collision operator

contains two terms corresponding to the elastic and inelastic collisions respectively. Where the relaxation process becomes $f \rightarrow f^{eq} \rightarrow g$, and the inelastic collision process from f^{eq} to g takes a much longer time $Z_r\tau$ than that of elastic collision process by τ . The additional term Q_s in the collision part accounts for the energy exchange between the translational and rotational energy, which contributes to the source term for the corresponding three-dimensional macroscopic flow evolution. The above three-dimensional extended BGK model is a natural extension for two-dimensional extended BGK model¹³.

The relation between mass ρ , momentum($\rho U, \rho V, \rho W$), total energy ρE , and rotational energy ρE_r with the distribution function f is given by,

$$W = \begin{pmatrix} \rho \\ \rho U \\ \rho V \\ \rho W \\ \rho E \\ \rho E_r \end{pmatrix} = \int \psi_\alpha f d\Xi, \quad \alpha = 1, 2, 3, 4, 5, 6, \quad (6)$$

where $d\Xi = dudvdwd\xi_r$ and ψ_α is the component of the vector of collision invariants

$$\psi = (\psi_1, \psi_2, \psi_3, \psi_4, \psi_5, \psi_6)^T = (1, u, v, w, \frac{1}{2}(u^2 + v^2 + w^2 + \xi_r^2), \frac{1}{2}\xi_r^2)^T.$$

As a new temperature λ_r is introduced, the constraint of rotational energy relaxation has to be imposed on the above extended kinetic model to self-consistently determine all unknowns. Since only mass, momentum and total energy are conserved during particle collisions, the compatibility condition for the collision term turns into,

$$\int \left(\frac{f^{eq} - f}{\tau} + Q_s \right) \psi_\alpha d\Xi = \mathbf{S} = (0, 0, 0, 0, 0, s)^T, \quad \alpha = 1, 2, 3, 4, 5, 6. \quad (7)$$

The source term for the rotational energy is from the energy exchange between translational and rotational ones during inelastic collision. The source term for the rotational energy is modeled through the Landau-Teller-Jeans-type relaxation model,

$$s = \frac{(\rho E_r)^{eq} - \rho E_r}{Z_r \tau}. \quad (8)$$

The equilibrium energy $(\rho E_r)^{eq}$ is determined by the assumption $T_r = T_t = T$, such that

$$(\rho E_r)^{eq} = \frac{\rho}{2\lambda_r^{eq}} \quad \text{and} \quad \lambda_r^{eq} = \frac{K+3}{4} \frac{\rho}{\rho E - \frac{1}{2}\rho(U^2 + V^2 + W^2)}.$$

Here, the collision number Zr is related to the ratio of elastic collision frequency to inelastic frequency. The particle collision time multiplied by a rotational collision number Z_r models the relaxation process for the rotational energy to equilibrate with the translational one. The value Z_r used in current study is given by,

$$Z_r = \frac{Z_r^\infty}{1 + (\pi^{3/2}/2)\sqrt{T^*/T} + (\pi + \pi^2/4)(T^*/T)},$$

where the quantity T^* is the characteristic temperature of intermolecular potential, and Z_r^∞ is the limiting value. Over a temperature range from $30K$ to $3000K$ for Nitrogen, the values $Z_r^\infty = 23.0$ and $T^* = 91.5K$ are used. The local temperature T in the above equation is the translational temperature. More advanced models for the energy relaxation are discussed in^{20,21}.

Using the intermediate state give by Eq.(5), with the frozen of rotational energy exchange the 1st-order Champan-Enskog expansion gives,

$$f = f^{eq} + Knf_1 = f^{eq} - \tau \left(\frac{\partial f^{eq}}{\partial t} + u \frac{\partial f^{eq}}{\partial x} + v \frac{\partial f^{eq}}{\partial y} + w \frac{\partial f^{eq}}{\partial z} \right). \quad (9)$$

The corresponding macroscopic non-equilibrium multi-temperature continuum equations in three-dimensions can be derived as the appendix, and the final form is given by,

$$\frac{\partial W}{\partial t} + \frac{\partial F}{\partial x} + \frac{\partial G}{\partial y} + \frac{\partial H}{\partial z} = \frac{\partial F_v}{\partial x} + \frac{\partial G_v}{\partial y} + \frac{\partial H_v}{\partial z} + \mathbf{S}, \quad (10)$$

with

$$W = \begin{pmatrix} \rho \\ \rho U \\ \rho V \\ \rho W \\ \rho E \\ \rho E_r \end{pmatrix} \quad F = \begin{pmatrix} \rho U \\ \rho U^2 + p \\ \rho UV \\ \rho UW \\ (\rho E + p)U \\ \rho E_r U \end{pmatrix} \quad G = \begin{pmatrix} \rho V \\ \rho UV \\ \rho V^2 + p \\ \rho VW \\ (\rho E + p)V \\ \rho E_r V \end{pmatrix} \quad H = \begin{pmatrix} \rho W \\ \rho UW \\ \rho VW \\ \rho W^2 + p \\ (\rho E + p)W \\ \rho E_r W \end{pmatrix},$$

and

$$F_v = \begin{pmatrix} 0 \\ \tau_{xx} \\ \tau_{xy} \\ \tau_{xz} \\ U\tau_{xx} + V\tau_{xy} + W\tau_{xz} + q_x \\ U\tau_{tr} + q_{rx} \end{pmatrix} \quad G_v = \begin{pmatrix} 0 \\ \tau_{yx} \\ \tau_{yy} \\ \tau_{yz} \\ U\tau_{yx} + V\tau_{yy} + W\tau_{yz} + q_y \\ V\tau_{tr} + q_{ry} \end{pmatrix}$$

$$H_v = \begin{pmatrix} 0 \\ \tau_{zx} \\ \tau_{zy} \\ \tau_{zz} \\ U\tau_{zx} + V\tau_{zy} + W\tau_{zz} + q_z \\ W\tau_{tr} + q_{rz} \end{pmatrix},$$

where $\rho E = \frac{1}{2}\rho(\mathbf{U}^2 + 3RT_t + KRT_r)$ is the total energy, and $\rho E_r = \rho RT_r$ with $K = 2$ is the rotational energy. The pressure p is related to the translational temperature as $p = \rho RT_t$.

Meanwhile, the viscous normal stress terms are

$$\begin{aligned}\tau_{xx} &= \tau p \left[2 \frac{\partial U}{\partial x} - \frac{2}{3} \left(\frac{\partial U}{\partial x} + \frac{\partial V}{\partial y} + \frac{\partial W}{\partial z} \right) \right] - \frac{\rho K}{2(K+3)} \frac{1}{Zr} \left(\frac{1}{\lambda_t} - \frac{1}{\lambda_r} \right), \\ \tau_{yy} &= \tau p \left[2 \frac{\partial V}{\partial y} - \frac{2}{3} \left(\frac{\partial U}{\partial x} + \frac{\partial V}{\partial y} + \frac{\partial W}{\partial z} \right) \right] - \frac{\rho K}{2(K+3)} \frac{1}{Zr} \left(\frac{1}{\lambda_t} - \frac{1}{\lambda_r} \right), \\ \tau_{zz} &= \tau p \left[2 \frac{\partial W}{\partial z} - \frac{2}{3} \left(\frac{\partial U}{\partial x} + \frac{\partial V}{\partial y} + \frac{\partial W}{\partial z} \right) \right] - \frac{\rho K}{2(K+3)} \frac{1}{Zr} \left(\frac{1}{\lambda_t} - \frac{1}{\lambda_r} \right),\end{aligned}$$

with viscous shear stress term given by,

$$\begin{aligned}\tau_{xy} &= \tau_{yx} = \tau p \left(\frac{\partial U}{\partial y} + \frac{\partial V}{\partial x} \right), \\ \tau_{xz} &= \tau_{zx} = \tau p \left(\frac{\partial U}{\partial z} + \frac{\partial W}{\partial x} \right), \\ \tau_{yz} &= \tau_{zy} = \tau p \left(\frac{\partial V}{\partial z} + \frac{\partial W}{\partial y} \right),\end{aligned}$$

and heat conduction terms are

$$\begin{aligned}q_x &= \tau p \left[\frac{K}{4} \frac{\partial}{\partial x} \left(\frac{1}{\lambda_r} \right) + \frac{5}{4} \frac{\partial}{\partial x} \left(\frac{1}{\lambda_t} \right) \right], \\ q_y &= \tau p \left[\frac{K}{4} \frac{\partial}{\partial y} \left(\frac{1}{\lambda_r} \right) + \frac{5}{4} \frac{\partial}{\partial y} \left(\frac{1}{\lambda_t} \right) \right], \\ q_z &= \tau p \left[\frac{K}{4} \frac{\partial}{\partial z} \left(\frac{1}{\lambda_r} \right) + \frac{5}{4} \frac{\partial}{\partial z} \left(\frac{1}{\lambda_t} \right) \right].\end{aligned}$$

The following terms are related to governing equation of rotational energy ρE_r as,

$$\begin{aligned}\tau_{rt} &= \frac{3\rho K}{4(K+3)} \frac{1}{Zr} \left(\frac{1}{\lambda_t} - \frac{1}{\lambda_r} \right), \\ q_{rx} &= \tau p \frac{K}{4} \frac{\partial}{\partial x} \frac{1}{\lambda_r}, \\ q_{ry} &= \tau p \frac{K}{4} \frac{\partial}{\partial y} \frac{1}{\lambda_r}, \\ q_{rz} &= \tau p \frac{K}{4} \frac{\partial}{\partial z} \frac{1}{\lambda_r}.\end{aligned}$$

The source term in Eq.(10) is given by,

$$\mathbf{S} = (0, 0, 0, 0, 0, \frac{(\rho E_r)^{eq} - \rho E_r}{Z_r \tau}).$$

Instead of the bulk viscosity term in the standard NS equations, a relaxation term between translational and rotational energy is obtained in the above equations to model the non-equilibrium process. The bulk viscosity term in NS equations,

$$\frac{2}{3} \frac{K}{K+3} \tau p (U_x + V_y + W_z),$$

is replaced by the temperature relaxation term in the above Eq.(10),

$$-\frac{\rho K}{2(K+3)} \frac{1}{Z_r} \left(\frac{1}{\lambda_t} - \frac{1}{\lambda_r} \right) = \frac{\rho R}{Z_r} \frac{K}{K+3} (T_r - T_t).$$

In the limiting case of small departures from equilibrium, the rotational energy equation becomes

$$(\rho E_r)_t + (\rho E_r U)_x + (\rho E_r V)_y + (\rho E_r W)_z = \frac{\rho R}{Z_r \tau} \frac{3}{K+3} (T_t - T_r),$$

and with the Euler approximation for the right hand side of the above equation, we have

$$T_t - T_r = -\frac{2}{3} Z_r \tau T (U_x + V_y + W_z).$$

Based on above equation, the normal bulk viscosity term can be exactly recovered, given by

$$\frac{2}{3} \frac{K}{K+3} \tau p (U_x + V_y + W_z) = \frac{\rho R}{Z_r} \frac{K}{K+3} (T_r - T_t).$$

With the above macroscopic modeling equations for a multi-temperature system, the non-equilibrium flow in the near continuum regime is modeled beyond the NS assumption. The bulk viscosity is replaced by a relaxation term between translational and rotational energy, which seems more physically meaningful than the bulk viscosity assumption^{12,13}, for the flows inside the shock layer or the hypersonic flow near isothermal boundary. However, we are supposed to keep in mind that the extended kinetic equation Eq.(4) will be directly used in the numerical scheme in the following part, instead of solving the nonlinear system Eq.(10).

III. HIGH-ORDER FINITE VOLUME NON-EQUILIBRIUM GAS-KINETIC SCHEME

The extended model proposed in the previous section is solved based on the conservative finite volume method GKS¹⁹. The numerical fluxes at cell interfaces are evaluated based on the general time-dependent gas distribution solution. In this paper, a high-order non-equilibrium finite volume GKS will be constructed, where the additional source term is dealt with fourth-order Simpson interpolation rule.

A. Three-dimensional finite volume scheme

Taking moments of Eq.(4) and integrating over the control volume $V_{ijk} = \bar{x}_i \times \bar{y}_j \times \bar{z}_k$ with $\bar{x}_i = [x_i - \frac{\Delta x}{2}, x_i + \frac{\Delta x}{2}]$, $\bar{y}_j = [y_j - \frac{\Delta y}{2}, y_j + \frac{\Delta y}{2}]$, $\bar{z}_k = [z_k - \frac{\Delta z}{2}, z_k + \frac{\Delta z}{2}]$, the three-dimensional non-equilibrium finite volume scheme can be written as

$$\begin{aligned} \frac{dW_{ijk}}{dt} = L(W_{ijk}) = & \frac{1}{|V_{ijk}|} \left[\int_{\bar{y}_j \times \bar{z}_k} (F_{i-1/2,j,k} - F_{i+1/2,j,k}) dydz \right. \\ & + \int_{\bar{x}_i \times \bar{z}_k} (G_{i,j-1/2,k} - G_{i,j+1/2,k}) dx dz + \int_{\bar{x}_i \times \bar{y}_j} (H_{i,j,k-1/2} - G_{i,j,k+1/2}) dx dy \\ & \left. + S_{ijk}, \right] \quad (11) \end{aligned}$$

where W_{ijk} is the cell averaged flow variables of mass, momentum, total energy, and rotational energy, and S_{ijk} is cell averaged source term for the rotational energy. All of them are averaged over control volume V_{ijk} and the volume of the numerical cell is $|V_{ijk}| = \Delta x \Delta y \Delta z$. Here, numerical fluxes in x - direction is presented as an example

$$\int_{\bar{y}_j \times \bar{z}_k} F_{i+1/2,j,k} dy dz = F_{\mathbf{x}_{i+1/2,j,k},t} \Delta y \Delta z. \quad (12)$$

Based on the fifth-order weighted essentially non-oscillatory scheme (WENO-JS)²² for the spatial reconstruction on the primitive flow variables, the reconstructed pointwise values and the spatial derivatives in normal and tangential direction can be obtained. In the smooth flow computation, the linear form of WENO-JS is adopted to reduce the dissipation. The numerical fluxes $F_{\mathbf{x}_{i+1/2,j,k},t}$ can be provided by the flow solvers, which can be evaluated by taking moments of the gas distribution function as

$$F_{\mathbf{x}_{i+1/2,j,k},t} = \int \psi_\alpha u f(\mathbf{x}_{i+1/2,j,k}, t, \mathbf{u}, \xi) d\Xi, \quad \alpha = 1, 2, 3, 4, 5, 6, \quad (13)$$

where $f(\mathbf{x}_{i+1/2,j,k}, t, \mathbf{u}, \xi)$ is based on the integral solution of BGK equation Eq.(4) at the cell interface

$$f(\mathbf{x}_{i+1/2,j,k}, t, \mathbf{u}, \xi_r) = \frac{1}{\tau} \int_0^t f^{eq}(\mathbf{x}', t', \mathbf{u}, \xi_r) e^{-(t-t')/\tau} dt' + e^{-t/\tau} f_0(-\mathbf{u}t, \xi_r), \quad (14)$$

where $\mathbf{x}_{i+1/2,j,k} = \mathbf{0}$ is the location of the cell interface, $\mathbf{u} = (u, v, w)$ is the particle velocity, $\mathbf{x}_{i+1/2,j,k} = \mathbf{x}' + \mathbf{u}(t - t')$ is the trajectory of particles. f_0 is the initial gas distribution, and f^{eq} is the corresponding intermediate equilibrium state as Eq.(5). f^{eq} and f_0 can be constructed as

$$f^{eq} = f_0^{eq}(1 + \bar{a}x + \bar{b}y + \bar{c}z + \bar{A}t),$$

and

$$f_0 = \begin{cases} f_l^{eq}[1 + (a_l x + b_l y + c_l z) - \tau(a_l u + b_l v + c_l w + A_l)], & x \leq 0, \\ f_r^{eq}[1 + (a_r x + b_r y + c_r z) - \tau(a_r u + b_r v + c_r w + A_r)], & x > 0, \end{cases}$$

where f_l^{eq} and f_r^{eq} are the initial gas distribution functions on both sides of a cell interface. f_0^{eq} is the initial equilibrium state located at cell interface, which can be determined through the compatibility condition

$$\int \psi_\alpha f_0^{eq} d\Xi = \int_{u>0} \psi_\alpha f_l^{eq} d\Xi + \int_{u<0} \psi_\alpha f_r^{eq} d\Xi, \quad \alpha = 1, 2, 3, 4, 5, 6.$$

For a second-order flux, the time-dependent gas distribution function at the cell interfaces is evaluated as

$$\begin{aligned} f(\mathbf{x}_{i+1/2,j,k}, t, \mathbf{u}, \xi_r) &= (1 - e^{-t/\tau})f_0^{eq} + ((t + \tau)e^{-t\tau} - \tau)(\bar{a}u + \bar{b}v + \bar{c}w)f_0^{eq} \\ &\quad + (t - \tau + \tau e^{-t\tau})\bar{A}f_0^{eq} \\ &\quad + e^{-t/\tau}f_l^{eq}[1 - (\tau + t)(a_l u + b_l v + c_l w) - \tau A_l](1 - H(u)) \\ &\quad + e^{-t/\tau}f_r^{eq}[1 - (\tau + t)(a_r u + b_r v + c_r w) - \tau A_r]H(u), \end{aligned} \quad (15)$$

where the coefficients in Eq.(15) can be determined by the spatial derivatives of macroscopic flow variables and the compatibility condition. For three-dimensional diatomic gas, the expansion of spatial variation $\partial f^{eq}/\partial x$ is given by,

$$\frac{\partial f^{eq}}{\partial x} = \frac{1}{\rho}(a_1 + a_2 u + a_3 v + a_4 w + a_5(u^2 + v^2 + w^2) + a_6 \xi_r^2) f^{eq} = \frac{1}{\rho} a f^{eq}, \quad (16)$$

where all the coefficients in Eq.(16) can be explicitly determined by the relation with the microscopic and macroscopic variables at the cell interface, i.e., $W = \int \psi_\alpha f^{eq} dudvdwd\xi_r$ and $\partial W/\partial x = (1/\rho) \int \psi_\alpha a f^{eq} dudvdwd\xi_r$, where $W = (\rho, \rho U, \rho V, \rho W, \rho E, \rho E_r)$ are the flow variables. The components of coefficients a in Eq.(16) can be expressed as

$$\begin{aligned} a_6 &= 2 \frac{\lambda_r^2}{K} \left(2 \frac{\partial(\rho E_r)}{\partial x} - \frac{1}{2} \frac{K}{\lambda_r} \frac{\partial \rho}{\partial x} \right), \\ a_5 &= \frac{2\lambda_t^2}{3} (B - 2UA_1 - 2VA_2 - 2WA_3), \\ a_4 &= 2\lambda_t A_3 - 2W a_5, \\ a_3 &= 2\lambda_t A_2 - 2V a_5, \\ a_2 &= 2\lambda_t A_1 - 2U a_5, \\ a_1 &= \frac{\partial \rho}{\partial x} - a_2 U - a_3 V - a_4 W - a_5 (U^2 + V^2 + W^2 + \frac{3}{\lambda_t}) - a_6 \frac{K}{2\lambda_r}, \end{aligned}$$

with the defined variables

$$\begin{aligned} B &= 2 \frac{\partial(\rho E - \rho E_r)}{\partial x} - (U^2 + V^2 + W^2 + \frac{3}{\lambda_t}) \frac{\partial \rho}{\partial x}, \\ A_1 &= \frac{\partial(\rho U)}{\partial x} - U \frac{\partial \rho}{\partial x}, \\ A_2 &= \frac{\partial(\rho V)}{\partial y} - V \frac{\partial \rho}{\partial x}, \\ A_3 &= \frac{\partial(\rho W)}{\partial z} - W \frac{\partial \rho}{\partial x}. \end{aligned}$$

In a similar way, the temporal variation of $\partial f^{eq}/\partial t$ can be expanded and the corresponding coefficients can be obtained from the compatibility condition for the Chapman-Enskog

expansion

$$\int \psi_\alpha \left(\frac{\partial f^{eq}}{\partial t} + u \frac{\partial f^{eq}}{\partial x} + v \frac{\partial f^{eq}}{\partial y} + w \frac{\partial f^{eq}}{\partial z} \right) d\Xi = 0,$$

where the above six equations uniquely determine six unknowns in A , i.e., $A = A_1 + A_2u + A_3v + A_4w + A_5(u^2 + v^2 + w^2) + A_6\xi_r^2$.

Here, the second-order accuracy in time can be achieved by one step integration, with the second-order gas-kinetic flux solver Eq.(15). Based on a higher-order expansion of the equilibrium state around a cell interface, the one-stage high-order GKS has been developed successfully²³. However, the one-stage gas-kinetic solver become very complicated, especially for three-dimensional multidimensional computations. In order to reduce the complexity of high-order scheme, the technique of a two-stage fourth-order method will be used here for the development of high-order scheme for non-equilibrium flow.

B. Two-stage high-order temporal discretization

In recent study, a two-stage fourth-order time-accurate discretization was developed for Lax-Wendroff flow solvers, particularly applied for hyperbolic equations with the generalized Riemann problem (GRP) solver¹⁴ and the GKS¹⁵. Such method provides a reliable framework to develop a high-order three-dimensional non-equilibrium GKS with a second-order flux function Eq.(15) only, where the source terms will be treated by high-order interpolation. Key point for this two-stage high-order method is to use the time derivative of a flux function. In order to obtain the time derivative of flux function at t_n and $t_* = t_n + \Delta t/2$, the flux function should be approximated as a linear function of time within a time interval.

According to the numerical fluxes at cell interface Eq.(13), the following notation is introduced

$$\mathbb{F}_{i+1/2,j,k}(W^n, \delta) = \int_{t_n}^{t_n+\delta} \mathbf{F}_{i+1/2,j,k}(W^n, t) dt = \int_{t_n}^{t_n+\delta} F_{\mathbf{x}_{i+1/2,j,k},t} dt. \quad (17)$$

In the time interval $[t_n, t_n + \Delta t/2]$, the flux is expanded as the following linear form

$$\mathbf{F}_{i+1/2,j,k}(W^n, t) = \mathbf{F}_{i+1/2,j,k}^n + \partial_t \mathbf{F}_{i+1/2,j,k}^n (t - t_n). \quad (18)$$

Based on Eq.(17) and linear expansion of flux as Eq.(18), the coefficients $\mathbf{F}_{i+1/2,j,k}(W^n, t_n)$ and $\partial_t \mathbf{F}_{i+1/2,j,k}(W^n, t_n)$ can be determined as,

$$\begin{aligned}\mathbf{F}_{i+1/2,j,k}(W^n, t_n)\Delta t + \frac{1}{2}\partial_t \mathbf{F}_{i+1/2,j,k}(W^n, t_n)\Delta t^2 &= \mathbb{F}_{i+1/2,j,k}(W^n, \Delta t), \\ \frac{1}{2}\mathbf{F}_{i+1/2,j,k}(W^n, t_n)\Delta t + \frac{1}{8}\partial_t \mathbf{F}_{i+1/2,j,k}(W^n, t_n)\Delta t^2 &= \mathbb{F}_{i+1/2,j,k}(W^n, \Delta t/2).\end{aligned}$$

By solving the linear system, we have

$$\begin{aligned}\mathbf{F}_{i+1/2,j,k}(W^n, t_n) &= (4\mathbb{F}_{i+1/2,j,k}(W^n, \Delta t/2) - \mathbb{F}_{i+1/2,j,k}(W^n, \Delta t))/\Delta t, \\ \partial_t \mathbf{F}_{i+1/2,j,k}(W^n, t_n) &= 4(\mathbb{F}_{i+1/2,j,k}(W^n, \Delta t) - \mathbb{F}_{i+1/2,j,k}(W^n, \Delta t/2))/\Delta t^2,\end{aligned}\tag{19}$$

and $\mathbf{F}_{i+1/2,j,k}(W^*, t_*)$, $\partial_t \mathbf{F}_{i+1/2,j,k}(W^*, t_*)$ for the intermediate state t_* can be constructed similarly.

With these notations, the three-dimensional high-order non-equilibrium algorithm for multi-temperature flow is given by

(i) With the initial reconstruction, update W^* at $t_* = t_n + \Delta t/2$ by

$$\begin{aligned}W_{ijk}^* &= W_{ijk}^n - \frac{1}{\Delta x} [\mathbb{F}_{i+1/2,j,k}(W^n, \Delta t/2) - \mathbb{F}_{i-1/2,j,k}(W^n, \Delta t/2)] \\ &\quad - \frac{1}{\Delta y} [\mathbb{G}_{i,j+1/2,k}(W^n, \Delta t/2) - \mathbb{G}_{i,j-1/2,k}(W^n, \Delta t/2)] \\ &\quad - \frac{1}{\Delta z} [\mathbb{H}_{i,j,k+1/2}(W^n, \Delta t/2) - \mathbb{H}_{i,j,k-1/2}(W^n, \Delta t/2)] \\ &\quad + S_{ijk}^* \frac{\Delta t}{2},\end{aligned}\tag{20}$$

and compute the fluxes and their derivatives by Eq.(19) for future use,

$$\begin{aligned}\mathbf{F}_{i+1/2,j,k}(W^n, t_n), \mathbf{G}_{i,j+1/2,k}(W^n, t_n), \mathbf{H}_{i,j,k+1/2}(W^n, t_n), \\ \partial_t \mathbf{F}_{i+1/2,j,k}(W^n, t_n), \partial_t \mathbf{G}_{i,j+1/2,k}(W^n, t_n), \partial_t \mathbf{H}_{i,j,k+1/2}(W^n, t_n).\end{aligned}$$

(ii) Reconstruct intermediate value W_{ijk}^* and compute

$$\partial_t \mathbf{F}_{i+1/2,j,k}(W^*, t_*), \partial_t \mathbf{G}_{i,j+1/2,k}(W^*, t_*), \partial_t \mathbf{H}_{i,j,k+1/2}(W^*, t_*),$$

where the derivatives are determined by Eq.(19) in the time interval $[t_*, t_* + \Delta t]$.

(iii) Update W_{ijk}^{n+1} by

$$\begin{aligned} W_{ijk}^{n+1} = & W_{ijk}^n - \frac{\Delta t}{\Delta x} [\mathcal{F}_{i+1/2,j,k}^n - \mathcal{F}_{i-1/2,j,k}^n] \\ & - \frac{\Delta t}{\Delta y} [\mathcal{G}_{i,j+1/2,k}^n - \mathcal{G}_{i,j-1/2,k}^n] - \frac{\Delta t}{\Delta z} [\mathcal{H}_{i,j,k+1/2}^n - \mathcal{H}_{i,j,k-1/2}^n] \\ & + S_{ijk}^{n+1} \Delta t, \end{aligned} \quad (21)$$

where $\mathcal{F}_{i+1/2,j,k}^n$, $\mathcal{G}_{i,j+1/2,k}^n$ and $\mathcal{H}_{i,j,k+1/2}^n$ are the numerical fluxes and expressed as

$$\begin{aligned} \mathcal{F}_{i+1/2,j,k}^n &= \mathbf{F}_{i+1/2,j,k}(W^n, t_n) + \frac{\Delta t}{6} [\partial_t \mathbf{F}_{i+1/2,j,k}(W^n, t_n) + 2\partial_t \mathbf{F}_{i+1/2,j,k}(W^*, t_*)], \\ \mathcal{G}_{i,j+1/2,k}^n &= \mathbf{G}_{i,j+1/2,k}(W^n, t_n) + \frac{\Delta t}{6} [\partial_t \mathbf{G}_{i,j+1/2,k}(W^n, t_n) + 2\partial_t \mathbf{G}_{i,j+1/2,k}(W^*, t_*)], \\ \mathcal{H}_{i,j,k+1/2}^n &= \mathbf{H}_{i,j,k+1/2}(W^n, t_n) + \frac{\Delta t}{6} [\partial_t \mathbf{H}_{i,j,k+1/2}(W^n, t_n) + 2\partial_t \mathbf{H}_{i,j,k+1/2}(W^*, t_*)], \end{aligned}$$

where S_{ijk}^* and S_{ijk}^{n+1} are source terms, which will be solved through a high-order semi-implicit way.

C. Fourth-order Simpson interpolation for source term

Let s_{ijk} denotes the source component for rotational energy ρE_r , while other components in source term S_{ijk} are zero. Here, ρE_r can be updated using an semi-implicit scheme based on fourth-order Simpson interpolation rule.

(i) Update $(\rho E_r)^*$ at $t^* = t_n + \Delta t/2$ by

$$\begin{aligned} (\rho E_r)_{ijk}^* &= (\rho E_r)_{ijk}^n + (RHS)_{ijk}^* + \frac{\Delta t^*}{2} (s_{ijk}^n + s_{ijk}^{n+1}), \\ s_{ijk}^n &= \frac{(\rho E_r^{eq})_{ijk}^n - (\rho E_r)_{ijk}^n}{(Z_r \tau)_{ijk}^n}, \\ s_{ijk}^* &= \frac{(\rho E_r^{eq})_{ijk}^* - (\rho E_r)_{ijk}^*}{(Z_r \tau)_{ijk}^*}, \end{aligned}$$

thus

$$(\rho E_r)_{ijk}^* = \frac{2(Z_r \tau)_{ijk}^*}{2(Z_r \tau)_{ijk}^* + \Delta t^*} [(\rho E_r)_{ijk}^n + (RHS)_{ijk}^* + \frac{\Delta t^*}{2} (s_{ijk}^n + \frac{(\rho E_r^{eq})_{ijk}^*}{(Z_r \tau)_{ijk}^*})], \quad (22)$$

where $\Delta t^* = \Delta t/2$ and $(RHS)_{ijk}^*$ represents the component for rotational energy on the right hand side of Eq.(20) without source term. $(\rho E_r)^*$ can be updated based on Eq.(22), as the right hand side terms are known after updating the flow variables through fluxes at t^* .

(ii) Update $(\rho E_r)^{n+1}$ at t^{n+1} by

$$\begin{aligned} (\rho E_r)_{ijk}^{n+1} &= (\rho E_r)_{ijk}^n + (RHS)_{ijk}^{n+1} + \frac{\Delta t}{6} (s_{ijk}^n + 4s_{ijk}^* + s_{ijk}^{n+1}), \\ s_{ijk}^{n+1} &= \frac{(\rho E_r^{eq})_{ijk}^{n+1} - (\rho E_r)_{ijk}^{n+1}}{(Z_r \tau)_{ijk}^{n+1}}, \end{aligned}$$

thus

$$(\rho E_r)_{ijk}^{n+1} = \frac{6(Z_r \tau)_{ijk}^{n+1}}{6(Z_r \tau)_{ijk}^{n+1} + \Delta t} [(\rho E_r)_{ijk}^n + (RHS)_{ijk}^{n+1} + \frac{\Delta t}{6} (s_{ijk}^n + 4s_{ijk}^* + \frac{(\rho E_r^{eq})_{ijk}^{n+1}}{(Z_r \tau)_{ijk}^{n+1}})], \quad (23)$$

where $(RHS)_{ijk}^{n+1}$ represents the component for rotational energy on the right hand side of Eq.(21) without source term. The right hand side terms in Eq.(23) are known after updating the flow variables through fluxes at t^{n+1} , so $(\rho E_r)^{n+1}$ can be updated based on the fourth-order Simpson interpolation rule.

IV. NUMERICAL EXAMPLES

In this section, numerical tests from smooth flow to hypersonic ones will be presented to validate our numerical scheme. The collision time τ takes

$$\tau = \frac{\mu}{p} + C \frac{|p_L - p_R|}{|p_L + p_R|} \Delta t,$$

where μ is the viscous coefficient obtained from Sutherland's Law, and C is set to 1.5 in the computation. p_L and p_R denotes the pressure on the left and right hand sides at the cell interface, which will reduce to $\tau = \mu/p$ in the smooth flow region. Δt is the time step which

is determined according to the CFL number, which takes 0.3 in these computations.

A. Decaying homogeneous isotropic turbulence

Decaying homogeneous isotropic turbulence (DHIT) provides a benchmark for testing the dissipative behavior of numerical scheme. In current study, the reference experiment is conducted by Comte-Bellot et al.²⁴, with Taylor Reynolds number $Re_\lambda = 71.6$ and turbulent Mach number $Ma_t = 0.2$. Here, computation domain is $(2\pi)^3$ box with 128^3 uniform grids. Vreemann-type large dddy simulation (LES) model²⁵ is implemented with periodic boundary condition in 6 faces.

The turbulent fluctuating velocity as u' , the Taylor microscale λ , the Taylor Reynolds number Re_λ and the turbulent Mach number Ma_t are defined as

$$\begin{aligned} u' &= \langle (u_1^2 + u_2^2 + u_3^2)/3 \rangle^{1/2}, \\ \lambda^2 &= \frac{u'^2}{\langle (\partial u_1 / \partial x_1)^2 \rangle}, \\ Re_\lambda &= \frac{u' \lambda}{\nu}, \\ Ma_t &= \frac{\langle u_1^2 + u_2^2 + u_3^2 \rangle^{1/2}}{c}, \end{aligned}$$

where $\langle \dots \rangle$ represents the space average in computation domain. c represents the local sound speed, and ν represents the kinematic viscosity coefficient as μ/ρ . The initial velocity fields is computed from experiments energy spectral, with constant pressure, density and temperature. For multi-temperature simulation, collision number $Z_r = 5$ is used. The rotational temperature is initiated with the same value as translational temperature. The following quantities of turbulence have been computed in our simulations

$$\begin{aligned} E(\kappa) &= \frac{1}{2} \int_{\kappa_{min}}^{\kappa_{max}} \Phi_{ii}(\boldsymbol{\kappa}) \delta(|\boldsymbol{\kappa}| - \kappa) d\boldsymbol{\kappa}, \\ M_{loc} &= \frac{(u_1^2 + u_2^2 + u_3^2)^{1/2}}{c}, \\ \Delta_T &= \frac{T_{rn} - R_{ot}}{T_0}, \end{aligned}$$

where velocity spectral Φ_{ii} is the Fourier transform of two-point correlation, with wave

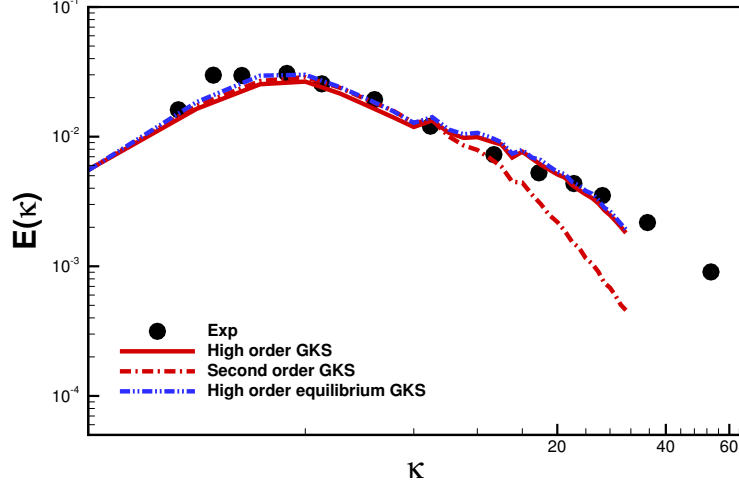


FIG. 1. Comparison of TKE spectral on high order equilibrium GKS, high order GKS and second order GKS with collision number $Z_r = 5$ at dimensionless time $t^* = 0.87$. The experimental data is from²⁴.

number $\kappa_{min} = 0$ and $\kappa_{max} = 64$. T_0 is the initial temperature, while T_{rn} and R_{ot} represent the translational temperature and rotational temperature, respectively.

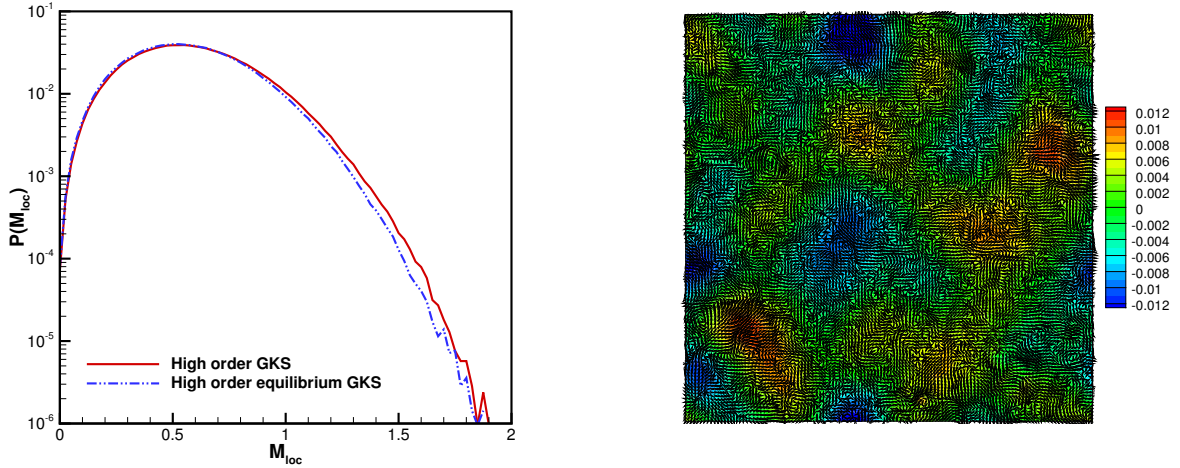


FIG. 2. PDF of the local Mach number M_{loc} (left) and contour of Δ_T (right) on the $z = 0.5$ plane at dimensionless time $t^* = 0.87$.

Figure 1 shows the turbulence kinetic energy (TKE) spectral at dimensionless time $t^* = 0.87$, based on high order equilibrium GKS, high order GKS and second order GKS. Without special statement, high order GKS denotes current high order non-equilibrium multi-temperature GKS. In high wavenumber region, TKE spectral from high order GKS is

closer to the experiment result, which outweighs results from second order GKS. High order accuracy is achieved in high order GKS, which has advantage of simulating non-equilibrium multi-temperature flow when smooth equilibrium region appears. Besides, tiny difference resulting from the different bulk viscosity term between high order equilibrium GKS and high order GKS is observed in this TKE spectral. This different behavior is also verified by the PDF of the local Mach number M_{loc} and the contours of Δ_T as the Figure 2, as the maximum difference between translational temperature and rotational temperature on the $z = 0.5$ plane at dimensionless time $t^* = 0.87$ is no more than 1.2%.

B. Low-density nozzle flow

Low-thrust rocket engine has been used for the control of altitude and trajectory of satellites and spacecrafts. For this type of rocket engine, the fluid experiences continuum, transition flow regime, which provides a necessary test for the validity of current high order GKS method for near continuum flow regime.

Low density nozzle flow has been measured using the electron beam fluorescence technique by Rothe²⁶, and DSMC simulations have been performed by Chung et al.²⁷. The flow condition for the test case is stagnation temperature $T_0 = 300K$, stagnation pressure $P_0 = 474Pa$, wall temperature $T_w = 300K$. This is an axis-symmetric flow problem, only one quarter part of this nozzle has been computed with $340 \times 60 \times 60$ grid points used inside the nozzle. Empirical first-order slip boundary condition²⁸ is used in current high order GKS method for isothermal boundary condition.

Figure 3 shows the Mach contour and non-dimensional density contour inside this nozzle, where high ratio of density from inlet to outlet are observed. The experimental data of density and rotational temperature along the nozzle centerline are shown in Figure 4. Current high order GKS method is validated in near continuum flow regime, as computation results provides a close match with the experimental measurement.

C. Rarefied hypersonic flow over a flat plate

Physical phenomena occurring around spacecraft in a hypersonic rarefied gas flow are studied in order to understand these phenomena and to design a real size vehicle. Following

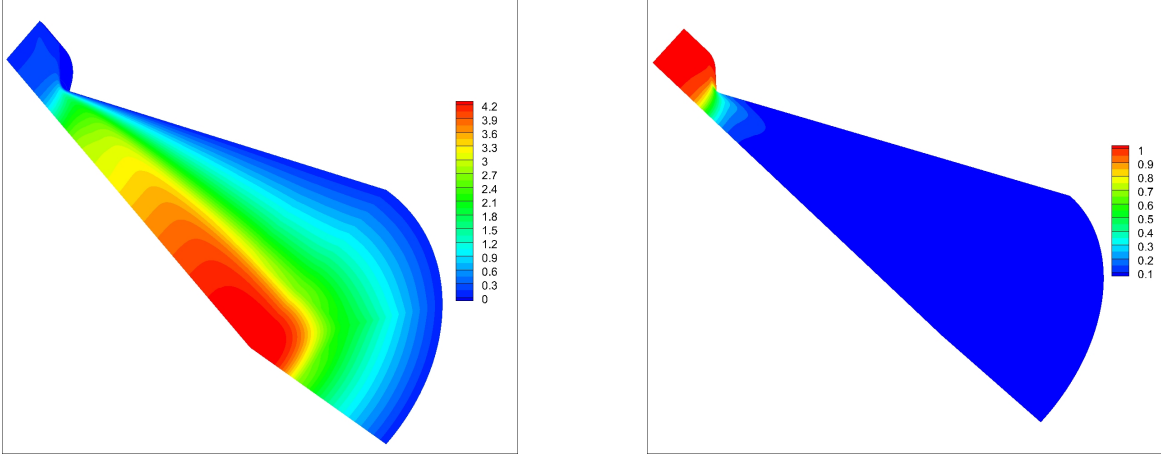


FIG. 3. Mach contour (left) and non-dimensional density contour (right) in the nozzle flow computations.

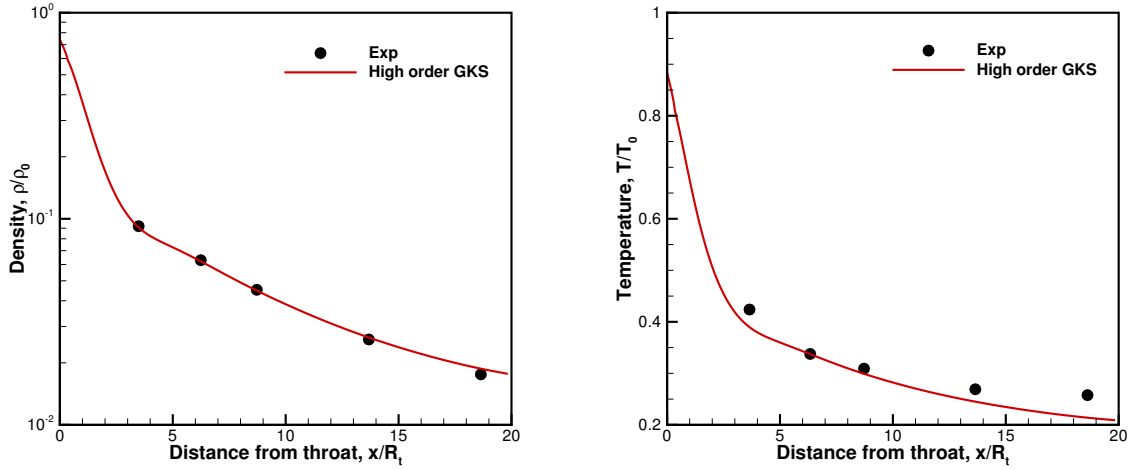


FIG. 4. Density and rotational temperature distributions along the central line of the nozzle, where R_t is the throat radius. The measured rotational temperature is from experiment²⁶.

the experiment conducted by Tsuboi et al²⁹, simulation on the hypersonic rarefied gas flow over a flat plate is implemented. The case is the run 34, with the nozzle exit Mach number $Ma = 4.89$, stagnation temperature $T_0 = 670K$, stagnation pressure $P_0 = 983Pa$, nozzle exit temperature $T_e = 116K$, and flat plate surface temperature $T_w = 290K$ with first-order slip boundary condition used. The geometry is shown in Fig 5, where 400×200 and 300×100 grid points above and below the flat plate are used. In this case, the shock wave and boundary layer interaction near a sharp leading edge caused non-equilibrium between translational and rotational temperatures in the rarefied gas regime.

The temperature distributions in the vertical direction above the flat plate at the locations

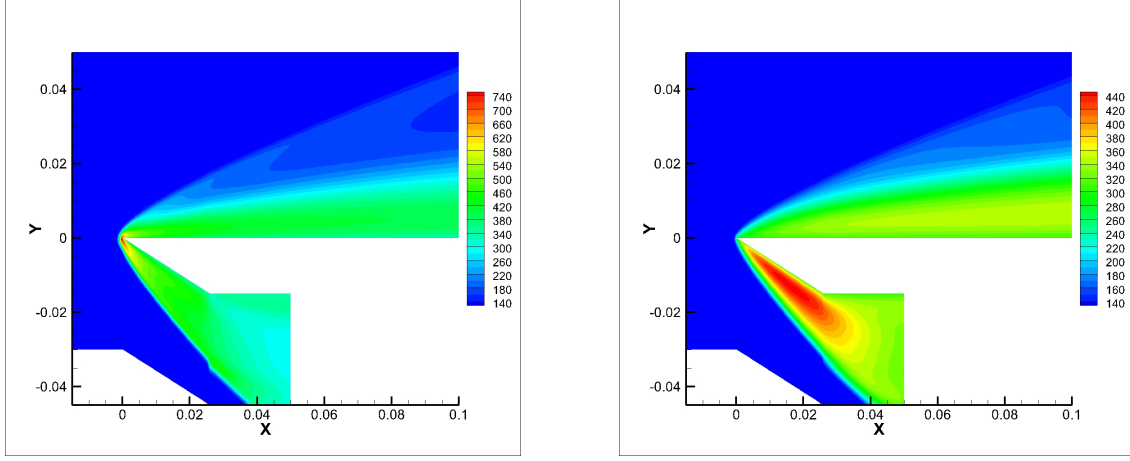


FIG. 5. Translational (left) and rotational (right) temperature contours in the hypersonic flow over a flat plate.

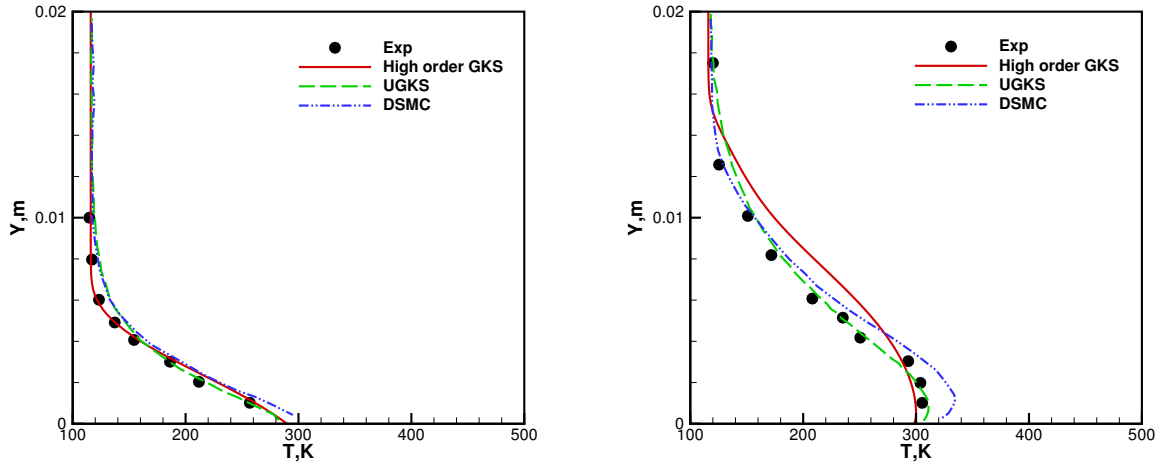


FIG. 6. Rotational temperature distributions in the vertical direction at $x = 5mm$ (left) and $x = 20mm$ (right). The measure rotational temperature²⁹, current high order GKS solutions, UGKS solution¹⁰, and DSMC solution²⁹ are presented.

of $x = 5mm$ and $x = 20mm$ from the leading edge are shown in Figure 6. As a comparison, the UGKS results¹⁰ and DSMC results²⁹ are also included. As shown in Figure 6, current high order GKS result is comparable with DSMC result, while current high order GKS is more efficient than DSMC. While, UGKS results have a perfect match with the experiment measurement than current high order GKS method and DSMC solution, which shows its great advantage of multi-scale properties for the whole flow regime simulation. Here coarse grids in physical space is used in UGKS scheme, with 59×39 grid points above the plate and 44×25 below the plate. However, velocity space is discretized with 80×60 grid points

in UGKS scheme, so current high order GKS method is still competitive in near continuum flow regime considering its higher efficiency than UGKS.

D. Type IV shock-shock interaction

Shock-shock interaction is the key issue in hypersonic flow. The presence of intense shock waves interaction strongly affects vehicle aerodynamic performance and leads to substantial localized aerodynamic heating. Shock-shock interaction was classified by Edney³⁰ into six patterns, depending on the impinging position and angle. In this paper, the type IV interaction is studied, which is the most severe case to form the hot spot on the surface of the cylinder due to the supersonic jet hitting on the wall. The flow patterns of the formation of a supersonic impinging jet, a series of shock waves, expansion waves, and shear layers in a local area of interaction, form a pretty challenging case for such a high-order GKS scheme.

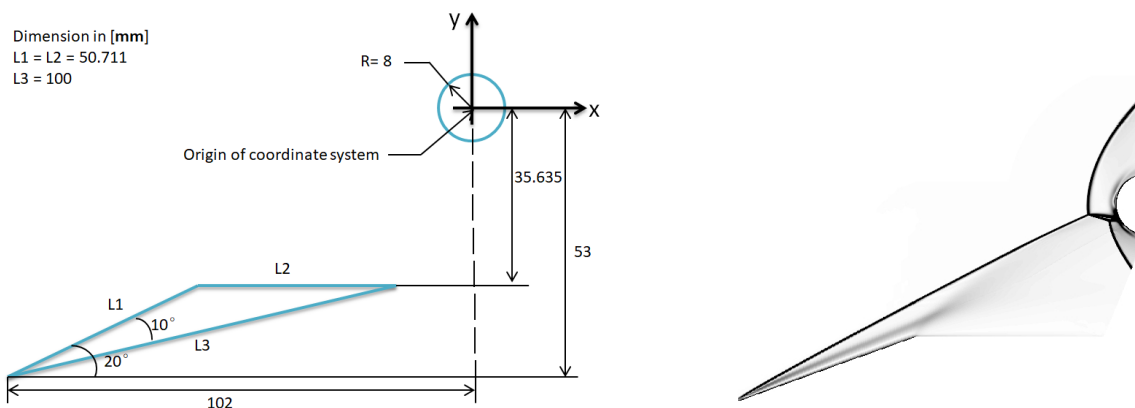


FIG. 7. Configuration for ONERA experiment³¹ (left) and Schlieren images by density gradient magnitude (right) from current high order GKS for type IV shock-shock interaction.

An experimental test has been conducted by Office national d'études et de recherches aérospatiales (ONERA)³¹ to investigate shock-shock interactions, which provides free-stream air flow properties of $M_\infty = 10$, $T_\infty = 52.5K$, $T_w = 300K$, and $Re_\infty/m = 1.66 \times 10^5$. The leading edge of the shock generator is positioned at a distance $L = 102mm$ upstream of the cylinder and $53mm$ below the axis of the cylinder, and the cylinder diameter is $16mm$. Our simulation is based on 250×440 grid points around the cylinder. Configuration for ONERA shock-shock interaction experiment and the Schlieren images by density gradient magnitude from current computational result are shown in Fig 7. A steady state solution is obtained

from the high order GKS scheme after a long time iteration with the iterative steps on the order of 10^5 and the flow structure keeps the same form.

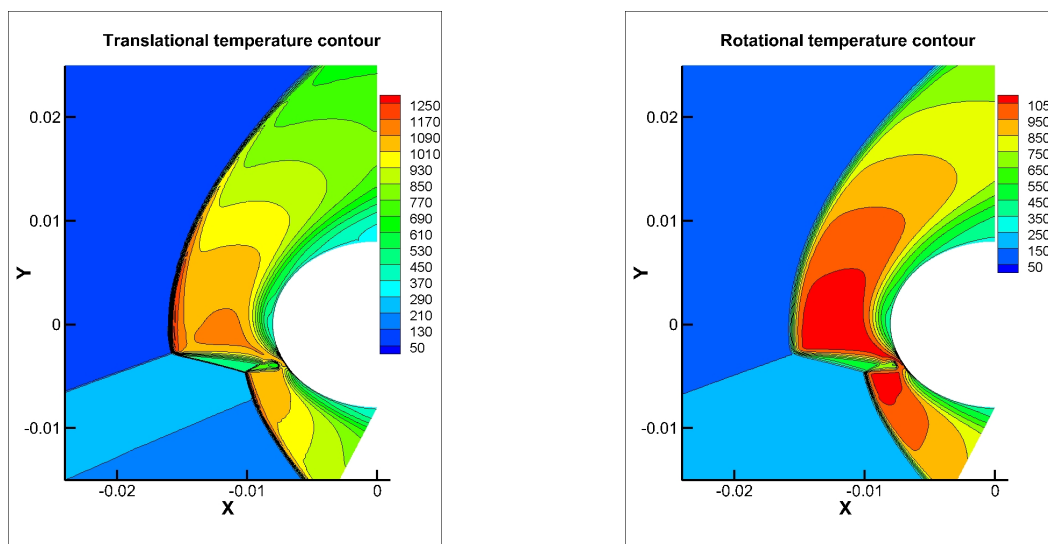


FIG. 8. Translational temperature contour (left) and rotational temperature contour (right) for type IV shock-shock interaction.

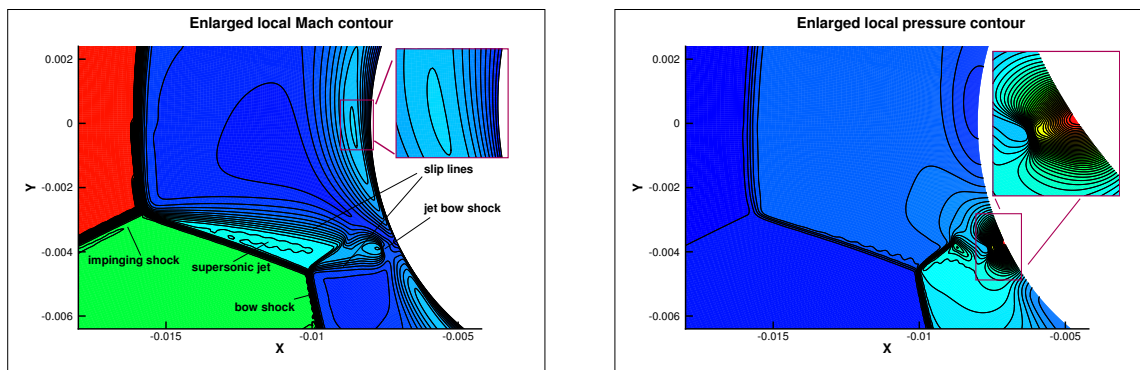


FIG. 9. Local Mach contour (left) and pressure (right) contour in the supersonic jet region.

The translational temperature contour and rotational temperature contour around the cylinder are shown in Fig 8. These contours confirm the existence of multiple temperature for this hypersonic flow. More specifically, the Mach number and pressure in the supersonic jet region are shown in Fig 9, which clearly shows the strong jet and hot spot around the cylinder surface. Figure 10 presents two horizontal profiles of measured rotational temperature in experiment. One is located above the upper shock triple point at $y = -2mm$, and the other is the line at $y = -4mm$, which passes the transmitted shock and intersects with the surface one degree below the location of jet impingement. The high-order GKS results are

close to DSMC solution³² at $y = -2mm$, while oscillation appears in DSMC simulation. At $y = -4mm$, our computational results have a closer match with the experiment than DSMC solution, especially near $x = 0mm$ region.

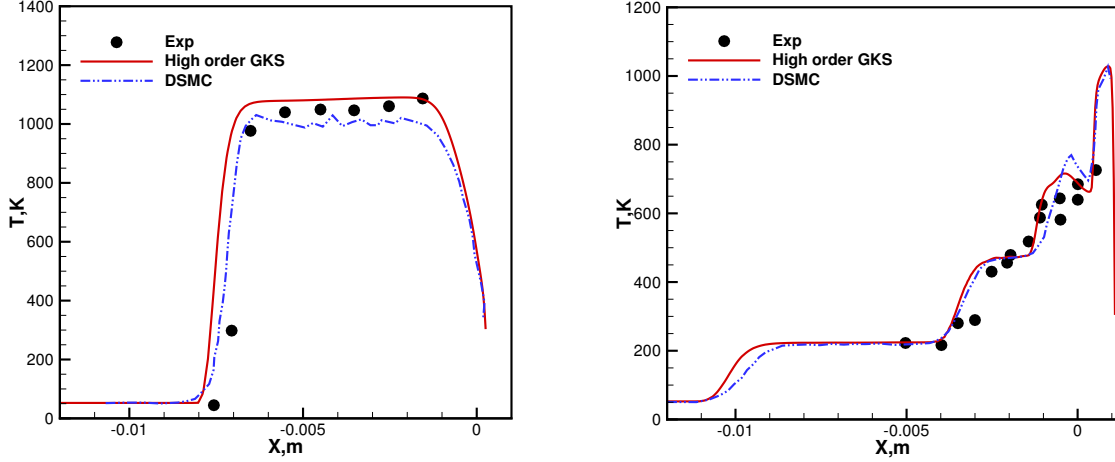


FIG. 10. Rotational temperature profile at $y = -2mm$ (left) and profile at $y = -4mm$ (right). The measured rotational temperature³¹, current high order GKS solutions, and DSMC solution³² are presented.

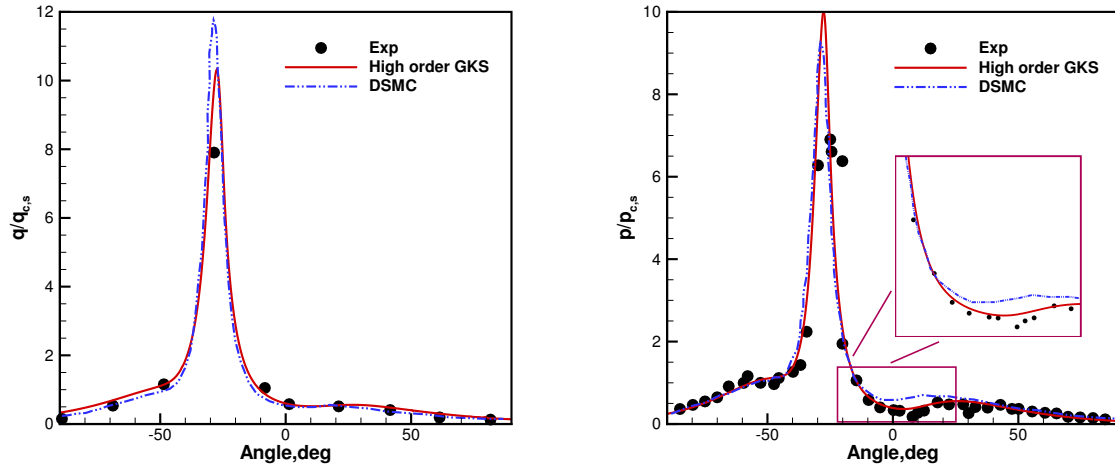


FIG. 11. Non-dimensional heating-rate distribution (left) and non-dimensional pressure distribution (right) along the cylindrical surface. The measured rotational temperature³¹, current high order GKS solutions, and DSMC solution³² are presented.

The non-dimensional pressure and heat flux along the cylindrical surface from experimental measurements³¹, the high order GKS and DSMC computational results³² are shown

in Fig 11, where $p_{c,s} = 760Pa$ and $q_{c,s} = 5.7W/cm^2$ are the reference value for undisturbed flow about cylinder. The experimental heating data set are inadequate to define the peak value because of the limited spatial resolution, while the high order GKS and DSMC present the close peak position with different peak values. In terms of pressure distribution, the high order GKS outweighs DSMC results near 0° . Near 0° region, a slightly low pressure region is found in Figure 9, which provides confidence on the high accuracy achieved by the high-order GKS scheme.

V. CONCLUSION

In this paper, a high-order three-dimensional multi-temperature GKS method is implemented under the two-stage fourth-order framework. Based on the extended BGK model, the three-dimensional macroscopic governing equations for diatomic gas are derived, which provide better insight into the behavior of the multi-temperature flow. Based on the developed multiple temperature kinetic model, a corresponding high-order GKS is constructed under the two-stage fourth-order framework and the source term discretization with fourth-order Simpson interpolation rule. For non-equilibrium multi-temperature flow computation, decaying homogeneous isotropic turbulence, nozzle flows, hypersonic rarefied flow over a plate, and type IV shock-shock interaction cases are tested. Comparisons among the numerical solutions from current high order GKS scheme, UGKS results, DSMC solutions, and experimental measurements show the high accuracy and quite robustness of current numerical method. Most importantly, the current finite volume gas-kinetic scheme updating the macroscopic flow variables explicitly, high efficiency is achieved in comparison with UGKS and DSMC methods, especially near the continuum flow region.

APPENDIX: CONNECTION BETWEEN BGK AND MACROSCOPIC NON-EQUILIBRIUM MULTI-TEMPERATURE EQUATIONS IN THREE-DIMENSIONS

Derivation of the Navier-Stokes and Euler equations from the BGK model can be found in the Appendix B in¹¹. For macroscopic non-equilibrium multi-temperature equations in two-

dimensions, it has been derived in¹³. This appendix provides the details for the derivation to macroscopic non-equilibrium multi-temperature equations in three-dimensions. In this appendix, "Eq.(B.x)" represents the preliminary equation in Appendix B¹¹, which will not be rewritten in current appendix.

Continuity equation is given by

$$\rho_{,t} + (\rho U_k)_{,k} = 0, \quad (\text{A.1})$$

which can be used to simplify the momentum equations, the total energy equations, and the rotational energy equations.

For momentum equations, the left side \mathcal{L}_5 in Eq.(B.2) can be grouped as

$$\begin{aligned} \mathcal{L}_5 = & \frac{1}{2} U_n^2 [\rho_{,t} + (\rho U_k)_{,k}] + \rho U_n U_{n,t} + \rho U_k U_n U_{n,k} + U_k p_{,k} \\ & + \frac{K+3}{2} [p_{,t} + U_k p_{,k}] + \frac{K+5}{2} p U_{k,k} + \frac{K}{2} (p_r - p)_t + \frac{K}{2} [(p_r - p) U_k]_{,k}. \end{aligned}$$

The first term is $\frac{1}{2} U_n^2 \mathcal{L}_1$ which is $\mathcal{O}(\epsilon^2)$, and next three are $U_n \mathcal{L}_n$, and are therefore $\mathcal{O}(\epsilon)$.

Then \mathcal{L}_5 can be rewritten as

$$\begin{aligned} \mathcal{L}_5 = & \frac{K+3}{2} [p_{,t} + U_k p_{,k}] + \frac{K+5}{2} p U_{k,k} + U_n \mathcal{L}_n \\ & + \frac{K}{2} \{ [(p_r)_t + (p_r U_k)_{,k}] - [p_{,t} + (p U_k)_{,k}] \}. \end{aligned} \quad (\text{A.2})$$

Based on the Chapman-Enskog expansion up to zero order, rotational energy equation is obtained as

$$(\rho E_r)_t + (\rho E_r U_k)_{,k} = \frac{3\rho}{2(K+3)Z_r\tau} \left(\frac{1}{\lambda_t} - \frac{1}{\lambda_r} \right), \quad (\text{A.3})$$

which can be used to eliminate $(p_r)_t + (p_r U_k)_{,k}$. Based on $p_r = \rho E_r$, Eq.(A.2) can be rewritten as,

$$\begin{aligned} -\frac{K+3}{2} [p_{,t} + U_k p_{,k}] = & \frac{K+5}{2} p U_{k,k} - \frac{K}{2} p U_{k,k} \\ & + \frac{K}{2} \left\{ \left[\frac{3}{2(K+3)Z_r\tau} \left(\frac{1}{\lambda_t} - \frac{1}{\lambda_r} \right) \right] - [p_{,t} + U_k p_{,k}] \right\} + U_n \mathcal{L}_n + \mathcal{O}(\epsilon). \end{aligned}$$

Finally, we get

$$p_{,t} + U_k p_{,k} = -\frac{5}{3} p U_{k,k} - \frac{K\rho}{2(K+3)Z_r\tau} \left(\frac{1}{\lambda_t} - \frac{1}{\lambda_r} \right) + \mathcal{O}(\epsilon), \quad (\text{A.4})$$

which can be used to eliminate $p_{,t} + U_k p_{,k}$.

For the right sides of the momentum equations, we consider

$$\mathcal{R}_j = (\hat{\tau} F_{jk})_{,k}.$$

Using the fact that all odd moments in w_k vanish, we get

$$\begin{aligned} F_{jk} &\equiv \langle u_j u_k \rangle_{,t} + \langle u_j u_k u_l \rangle_{,l} \\ &= U_j [(\rho U_k)_{,t} + [(\rho U_k U_l) + p \delta_{kl}]_{,l}] + \rho U_k U_{j,t} + (p \delta_{jk})_{,t} \\ &\quad + (\rho U_k U_l + p \delta_{kl}) U_{j,l} + (U_l p \delta_{jk} + U_k p \delta_{jl})_{,l}. \end{aligned}$$

The term in square brackets multiplying U_j is \mathcal{L}_k , i.e. it is $\mathcal{O}(\epsilon)$, and can therefore be ignored. Then, after gathering terms with coefficients U_k and p , we have

$$F_{jk} = U_k [\rho U_{j,t} + \rho U_l U_{j,l} + p_{,j}] + p [U_{k,j} + U_{j,k} + U_{l,l} \delta_{jk}] + \delta_{jk} [p_{,t} + U_l p_{,l}].$$

The coefficient of U_k is \mathcal{L}_j , according to Eq.(B.7), and can therefore be neglected. To eliminate $p_{,t}$ from the last term we use the Eq.(A.4) for \mathcal{L}_5 . Finally, decompose the tensor $U_{k,j}$ into its dilation and shear parts in the usual way, which gives

$$F_{jk} = [U_{k,j} + U_{j,k} - \frac{2}{3} U_{l,l} \delta_{jk}] - \frac{K\rho}{2(K+3)Z_r} \left(\frac{1}{\lambda_t} - \frac{1}{\lambda_r} \right) \delta_{jk}. \quad (\text{A.5})$$

Analogy to derive the Navier-Stokes total energy equation, we write

$$N_k \equiv \langle u_k \frac{u_n^3 + \xi_r^2}{2} \rangle_{,t} + \langle u_k u_l \frac{u_n^3 + \xi_r^2}{2} \rangle_{,l}.$$

which can be written as

$$N_k = N_k^{(1)} + N_k^{(2)}.$$

where

$$N_k^{(1)} = [U_k \frac{u_n^3 + \xi_r^2}{2}]_{,t} + [U_k \langle u_l \frac{u_n^3 + \xi_r^2}{2} \rangle]_{,l}.$$

and

$$N_k^{(2)} \equiv \langle w_k \frac{u_n^3 + \xi_r^2}{2} \rangle_{,t} + \langle w_k u_l \frac{u_n^3 + \xi_r^2}{2} \rangle_{,l}.$$

For $N_k^{(1)}$, we have

$$\begin{aligned} N_k^{(1)} &= U_k [\frac{1}{2} \langle u_n^2 + \xi_r^2 \rangle_{,t} + \frac{1}{2} \langle u_l (u_n^2 + \xi_r^2) \rangle_{,l}] \\ &+ [\frac{1}{2} \rho U_n^2 + \frac{K+3}{2} p] U_{k,t} + [U_l (\frac{1}{2} \rho U_n^2 + \frac{K+5}{2} p)] U_{k,l} \\ &+ \frac{K}{2} (p_r - p) U_{k,t} + \frac{K}{2} U_l (p_r - p) U_{k,l}. \end{aligned}$$

The coefficient of U_k in the equation above is \mathcal{L}_5 , and therefore can be dropped, and the remaining terms can be rewritten as

$$N_k^{(1)} = [\frac{1}{2} \rho U_n^2 + \frac{K+3}{2} p] [U_{k,t} + U_l U_{k,l}] + p U_l U_{k,l}.$$

According to equation Eq.(B.7) to eliminate $U_{k,t}$, we get

$$\begin{aligned} N_k^{(1)} &= -[\frac{1}{2} U_n^2 + \frac{K+3}{2} \frac{p}{\rho}] p_{,k} + p U_l U_{k,l} \\ &+ \frac{K}{2} (p_r - p) U_{k,t} + \frac{K}{2} U_l (p_r - p) U_{k,l}. \end{aligned} \tag{A.6}$$

For $N_k^{(2)}$, remembering that moments odd in w_k vanish, we have

$$\begin{aligned} N_k^{(2)} &= \langle U_n w_n w_k \rangle_{,t} + \langle U_l U_n w_n w_k \rangle_{,l} + \frac{1}{2} \langle U_n^2 w_k w_l \rangle_{,l} + \frac{1}{2} \langle w_k w_l (w_n^2 + \xi_r^2) \rangle_{,l} \\ &= (p U_k)_{,t} + (p U_k U_l)_{,l} + \frac{1}{2} (U_n^2 p)_{,k} + \frac{K+5}{2} (\frac{p^2}{\rho})_{,k} + \frac{K}{2} (\frac{p(p_r - p)}{\rho})_{,k}. \end{aligned}$$

This result can be written as

$$\begin{aligned}
N_k^{(2)} &= p[U_{k,t} + U_l U_{k,l} + U_k U_{l,l} + U_l U_{l,k}] \\
&\quad + U_k(p_{,t} + U_l p_{,l}) + \frac{1}{2} U_n^2 p_{,k} + \frac{K+5}{2} \left(\frac{p^2}{\rho}\right)_{,k} \\
&\quad + \frac{K}{2} \left(\frac{p(p_r - p)}{\rho}\right)_{,k}.
\end{aligned}$$

We want to eliminate the first order time derivative, so we rearrange above equality as

$$\begin{aligned}
N_k^{(2)} &= p[U_{k,t} + U_l U_{k,l} + U_k U_{l,l} + U_l U_{l,k}] \\
&\quad + U_k(p_{,t} + U_l p_{,l}) + \frac{1}{2} U_n^2 p_{,k} + \frac{K+5}{2} \left(\frac{p^2}{\rho}\right)_{,k} \\
&\quad + \frac{K}{2} \left(\frac{p(p_r - p)}{\rho}\right)_{,k}.
\end{aligned}$$

The $U_{k,t}$ can be eliminated by Eq.(B.7), and $p_{,t} + U_l p_{,l}$ can be eliminate by equation Eq.(A.4).

Hence

$$\begin{aligned}
N_k^{(2)} &= p[U_k U_{l,l} - \frac{p_{,k}}{\rho} + U_l U_{l,k}] \\
&\quad + U_k \left[-\frac{5}{3} p U_{l,l} - \frac{K}{(K+3)Z_r \tau} (p - p_r) \right] + \frac{1}{2} U_n^2 p_{,k} \\
&\quad + \frac{K+5}{2} \left(\frac{p^2}{\rho}\right)_{,k} + \frac{K}{2} \left(\frac{p(p_r - p)}{\rho}\right)_{,k}.
\end{aligned} \tag{A.7}$$

For N_k , sum up $N_k^{(1)}$ and $N_k^{(2)}$ together, obtaining

$$\begin{aligned}
N_k &= p[U_l(U_{k,l} + U_{l,k}) - \frac{2}{3} U_k U_{l,l}] - U_k \frac{K}{(K+3)Z_r \tau} (p - p_r) \\
&\quad + \frac{K+5}{2} p \left(\frac{p}{\rho}\right)_{,k} + \frac{K}{2} (p_r - p) U_{k,t} + \frac{K}{2} U_l (p_r - p) U_{k,l} + \frac{K}{2} \left(\frac{p(p_r - p)}{\rho}\right)_{,k}.
\end{aligned}$$

Eliminate $U_{k,t}$ by Eq.(B.7) again, leading to

$$\begin{aligned}
N_k &= p[U_l(U_{k,l} + U_{l,k}) - \frac{2}{3} U_k U_{l,l}] - U_k \frac{K}{(K+3)Z_r \tau} (p - p_r) \\
&\quad + \frac{K}{2} p \left(\frac{p_r}{\rho}\right)_{,k} + \frac{5}{2} p \left(\frac{p}{\rho}\right)_{,k}.
\end{aligned} \tag{A.8}$$

For rotational energy equation, multiplying the continuity equation Eq.(A.1) by $\frac{K}{4\lambda_r}$ and the subtracting the result from Eq.(A.3) gives,

$$\mathcal{L}_6 = \rho\left(\frac{K}{4\lambda_r}\right)_t + \rho U_k\left(\frac{K}{4\lambda_r}\right)_k - \frac{3\rho K}{4(K+3)Z_r\tau}\left(\frac{1}{\lambda_t} - \frac{1}{\lambda_r}\right) + \mathcal{O}(\epsilon^2). \quad (\text{A.9})$$

Unfolding \mathcal{R}_6 , leads to

$$\begin{aligned} \mathcal{R}_6 &= \frac{\partial}{\partial x_k} \left\{ \hat{\tau} \left[\left\langle \frac{1}{2} \xi_r^2 u_k \right\rangle_{,t} + \left\langle \frac{1}{2} \xi_r^2 u_k u_l \right\rangle_{,l} \right] \right\} \\ &= \hat{\tau} \left\{ \frac{K}{4\lambda_r} \left[(\rho U_k)_{,t} + (\rho U_k U_l + p \delta_{k,l})_{,l} \right] \right. \\ &\quad \left. + \rho U_k \left(\frac{K}{4\lambda_r}\right)_t + \left(\frac{K}{4\lambda_r}\right)_{,l} [\rho U_k U_l + p \delta_{kl}] \right\}_{,k}. \end{aligned}$$

The term in square brackets is \mathcal{L}_k , i.e. $\mathcal{O}(\epsilon)$, and can be dropped. Gathering terms with coefficients U_k and p , and eliminating $\rho\left(\frac{K}{4\lambda_r}\right)_t + \rho U_l\left(\frac{K}{4\lambda_r}\right)_{,l}$ by Eq.(A.9), we have

$$\begin{aligned} \mathcal{R}_6 &= \hat{\tau} \left\{ U_k \left[\rho \left(\frac{K}{4\lambda_r}\right)_t + \rho U_l \left(\frac{K}{4\lambda_r}\right)_{,l} \right] + \left(\frac{K}{4\lambda_r}\right)_{,l} p \delta_{kl} \right\}_{,k} \\ &= \hat{\tau} \left\{ U_k \left[\frac{3\rho K}{4(K+3)Z_r\tau} \left(\frac{1}{\lambda_t} - \frac{1}{\lambda_r}\right) \right] + \left(\frac{K}{4\lambda_r}\right)_{,l} p \delta_{kl} \right\}_{,k}. \quad (\text{A.10}) \end{aligned}$$

Above equations can be rewritten in the form of Eq.(10). Hence, macroscopic non-equilibrium multi-temperature equations to three-dimensions have been derived.

ACKNOWLEDGMENTS

We would like to thank Xing Ji, providing the helpful discussion and suggestions. The authors would like to thank TianHe-II in Guangzhou for providing high performance computational resources. The current research is supported by HongKong research grant council (16207715, 16206617) and National Science Foundation of China (11772281, 91530319).

REFERENCES

- ¹MS Ivanov and SF Gimelshein. Computational hypersonic rarefied flows. *Annual Review of Fluid Mechanics*, 30(1):469–505, 1998.

- ²GA Bird. Monte carlo simulation of gas flows. *Annual Review of Fluid Mechanics*, 10(1):11–31, 1978.
- ³GA Bird. Molecular gas dynamics and the direct simulation monte carlo of gas flows. *Clarendon, Oxford*, 508:128, 1994.
- ⁴JY Yang and JC Huang. Rarefied flow computations using nonlinear model boltzmann equations. *Journal of Computational Physics*, 120(2):323–339, 1995.
- ⁵Luc Mieussens. Discrete-velocity models and numerical schemes for the boltzmann-bgk equation in plane and axisymmetric geometries. *Journal of Computational Physics*, 162(2):429–466, 2000.
- ⁶VI Kolobov, RR Arslanbekov, VV Aristov, AA Frolova, and Sergey A Zabelok. Unified solver for rarefied and continuum flows with adaptive mesh and algorithm refinement. *Journal of Computational Physics*, 223(2):589–608, 2007.
- ⁷Zhi-Hui Li and Han-Xin Zhang. Gas-kinetic numerical studies of three-dimensional complex flows on spacecraft re-entry. *Journal of Computational Physics*, 228(4):1116–1138, 2009.
- ⁸Kun Xu and Juan-Chen Huang. A unified gas-kinetic scheme for continuum and rarefied flows. *Journal of Computational Physics*, 229(20):7747–7764, 2010.
- ⁹Juan-Chen Huang, Kun Xu, and Pubing Yu. A unified gas-kinetic scheme for continuum and rarefied flows iii: Microflow simulations. *Communications in Computational Physics*, 14(5):1147–1173, 2013.
- ¹⁰Sha Liu, Pubing Yu, Kun Xu, and Chengwen Zhong. Unified gas-kinetic scheme for diatomic molecular simulations in all flow regimes. *Journal of Computational Physics*, 259:96–113, 2014.
- ¹¹Kun Xu. *Direct modeling for computational fluid dynamics: construction and application of unified gas-kinetic schemes*. World Scientific, 2015.
- ¹²Kun Xu and Eswar Josyula. Continuum formulation for non-equilibrium shock structure calculation. *Communications in computational physics*, 1(3):425–448, 2006.
- ¹³Kun Xu, Xin He, and Chunpei Cai. Multiple temperature kinetic model and gas-kinetic method for hypersonic non-equilibrium flow computations. *Journal of computational physics*, 227(14):6779–6794, 2008.
- ¹⁴Jiequan Li and Zhifang Du. A two-stage fourth order time-accurate discretization for lax-wendroff type flow solvers i. hyperbolic conservation laws. *SIAM Journal on Scientific*

- Computing*, 38(5):A3046–A3069, 2016.
- ¹⁵Liang Pan, Kun Xu, Qibing Li, and Jiequan Li. An efficient and accurate two-stage fourth-order gas-kinetic scheme for the euler and navier–stokes equations. *Journal of Computational Physics*, 326:197–221, 2016.
- ¹⁶Prabhu Lal Bhatnagar, Eugene P Gross, and Max Krook. A model for collision processes in gases. i. small amplitude processes in charged and neutral one-component systems. *Physical review*, 94(3):511, 1954.
- ¹⁷Sydney Chapman, Thomas George Cowling, and David Burnett. *The mathematical theory of non-uniform gases: an account of the kinetic theory of viscosity, thermal conduction and diffusion in gases*. Cambridge university press, 1990.
- ¹⁸Taku Ohwada and Kun Xu. The kinetic scheme for the full-burnett equations. *Journal of computational physics*, 201(1):315–332, 2004.
- ¹⁹Kun Xu. A gas-kinetic bgk scheme for the navier–stokes equations and its connection with artificial dissipation and godunov method. *Journal of Computational Physics*, 171(1):289–335, 2001.
- ²⁰JG Parker. Rotational and vibrational relaxation in diatomic gases. *The Physics of Fluids*, 2(4):449–462, 1959.
- ²¹Katsuhisa Koura. Statistical inelastic cross-section model for the monte carlo simulation of molecules with discrete internal energy. *Physics of Fluids A: Fluid Dynamics*, 4(8):1782–1788, 1992.
- ²²Guang-Shan Jiang and Chi-Wang Shu. Efficient implementation of weighted eno schemes. *Journal of computational physics*, 126(1):202–228, 1996.
- ²³Qibing Li, Kun Xu, and Song Fu. A high-order gas-kinetic navier–stokes flow solver. *Journal of Computational Physics*, 229(19):6715–6731, 2010.
- ²⁴Genevieve Comte-Bellot and Stanley Corrsin. Simple eulerian time correlation of full- and narrow-band velocity signals in grid-generated, isotropic turbulence. *Journal of Fluid Mechanics*, 48(2):273–337, 1971.
- ²⁵AW Vreman. An eddy-viscosity subgrid-scale model for turbulent shear flow: Algebraic theory and applications. *Physics of fluids*, 16(10):3670–3681, 2004.
- ²⁶Dietmar E Rothe. Electron-beam studies of viscous flow in supersonic nozzles. *AIAA Journal*, 9(5):804–811, 1971.
- ²⁷Chan-Hong Chung, Suk C Kim, Robert M Stubbs, and Kenneth J De Witt. Low-density

- nozzle flow by the direct simulation monte carlo and continuum methods. *Journal of Propulsion and Power*, 11(1):64–70, 1995.
- ²⁸James Clerk Maxwell. Vii. on stresses in rarified gases arising from inequalities of temperature. *Philosophical Transactions of the royal society of London*, 170:231–256, 1879.
- ²⁹Nobuyuki Tsuboi and Yoichiro Matsumoto. Experimental and numerical study of hypersonic rarefied gas flow over flat plates. *AIAA journal*, 43(6):1243–1255, 2005.
- ³⁰Barry Edney. Anomalous heat transfer and pressure distributions on blunt bodies at hypersonic speeds in the presence of an impinging shock. Technical report, Flygtekniska Forsöksanstalten, Stockholm (Sweden), 1968.
- ³¹T Pot, B Chanetz, M Lefebvre, and P Bouchardy. Fundamental study of shock/shock interference in low density flow- flowfield measurements by dlcars. In *Rarefied Gas Dynamics Symposium, 21 st, Marseille, France, July 26-31, 1998, ONERA, TP*, number 1998-140, 1998.
- ³²JN Moss, T Pot, B Chanetz, and M Lefebvre. Dsmc simulation of shock/shock interactions: emphasis on type iv interactions. 1999.